



Microscale Self-Assembled Electrical Contacts

by Christopher J. Morris

ARL-TR-4298

September 2007

NOTICES

Disclaimers

The findings in this report are not to be construed as an official Department of the Army position unless so designated by other authorized documents.

Citation of manufacturer's or trade names does not constitute an official endorsement or approval of the use thereof.

Destroy this report when it is no longer needed. Do not return it to the originator.

Army Research Laboratory

Aberdeen Proving Ground, MD 21005-5066

ARL-TR-4298

September 2007

Microscale Self-Assembled Electrical Contacts

Christopher J. Morris

Sensors and Electron Devices Directorate, ARL

REPORT DOCUMENTATION PAGE			<i>Form Approved</i> OMB No. 0704-0188		
Public reporting burden for this collection of information is estimated to average 1 hour per response, including the time for reviewing instructions, searching existing data sources, gathering and maintaining the data needed, and completing and reviewing the collection information. Send comments regarding this burden estimate or any other aspect of this collection of information, including suggestions for reducing the burden, to Department of Defense, Washington Headquarters Services, Directorate for Information Operations and Reports (0704-0188), 1215 Jefferson Davis Highway, Suite 1204, Arlington, VA 22202-4302. Respondents should be aware that notwithstanding any other provision of law, no person shall be subject to any penalty for failing to comply with a collection of information if it does not display a currently valid OMB control number. PLEASE DO NOT RETURN YOUR FORM TO THE ABOVE ADDRESS.					
1. REPORT DATE (DD-MM-YYYY) September 2007		2. REPORT TYPE Final		3. DATES COVERED (From - To)	
4. TITLE AND SUBTITLE Microscale Self-Assembled Electrical Contacts			5a. CONTRACT NUMBER		
			5b. GRANT NUMBER		
			5c. PROGRAM ELEMENT NUMBER		
6. AUTHOR(S) Christopher J. Morris			5d. PROJECT NUMBER		
			5e. TASK NUMBER		
			5f. WORK UNIT NUMBER		
7. PERFORMING ORGANIZATION NAME(S) AND ADDRESS(ES) U.S. Army Research Laboratory Sensors and Electron Devices Directorate ATTN: AMSRD-ARL-SE-RL Aberdeen Proving Ground, MD 21005-5066			8. PERFORMING ORGANIZATION REPORT NUMBER ARL-TR-4298		
9. SPONSORING/MONITORING AGENCY NAME(S) AND ADDRESS(ES) U.S. Army Research Laboratory 2800 Powder Mill Road Adelphi, MD 20783-1197			10. SPONSOR/MONITOR'S ACRONYM(S)		
			11. SPONSOR/MONITOR'S REPORT NUMBER(S) ARL-TR-4298		
12. DISTRIBUTION/AVAILABILITY STATEMENT Approved for public release; distribution is unlimited.					
13. SUPPLEMENTARY NOTES					
14. ABSTRACT Self-assembly, or the spontaneous organization of parts into larger structures via energy minimization, is an attractive solution to overcome packaging and integration challenges. Capillary forces from a molten alloy can be used to both bond microscale components and make electrical connections between them in a self-assembly process. This report presents a systematic study of a number of metal alloys and self-assembly media with the aim of reducing the metal contact size between microscale components. Six different alloys or pure metals with melting points below 160 °C and nine different fluids with boiling points over 160 °C are considered. Tin-based alloys were generally found to be highly susceptible to corrosion at elevated temperatures above the alloy melting point, with Sn being the primary component to corrode and react with the underlying base metal. Using a eutectic Sn-Bi alloy and glycerol at 180–200 °C, the self-assembly of 1500 100-µm parts and 500 40-µm parts was demonstrated, each in about 2.5 min. Thus, 40 µm square, 4 µm high contacts were shown to remain functional for self-assembly. The electrical conductance of self-assembled 20 µm diameter, 2.5 µm high alloy contacts based on this Sn-Bi-glycerol system was measured at 1.9 /mΩ-cm ² .					
15. SUBJECT TERMS Self-assembly, capillary forces, eutectic Bi-Sn solder, packaging					
16. SECURITY CLASSIFICATION OF:			17. LIMITATION OF ABSTRACT SAR	18. NUMBER OF PAGES 38	19a. NAME OF RESPONSIBLE PERSON Christopher J. Morris
					19b. TELEPHONE NUMBER (Include area code) (301) 394-0950
a. REPORT U	b. ABSTRACT U	c. THIS PAGE U			

Contents

List of Figures	iv
List of Tables	v
Acknowledgement	vi
1. Introduction	1
2. Alloy and Fluid Environment Experiments	3
2.1 Methods	3
2.2 Results and Discussion	6
3. Self-Assembly	13
3.1 Methods	13
3.2 Results and Discussion	16
3.3 Verification of Electrical Connectivity	21
4. Conclusion and Future Directions	22
References	24
Acronyms	28
Distribution List	30

List of Figures

Figure 1. Schematic drawing showing how one part from a randomly agitated collection of parts will assemble on a molten alloy-coated binding site, where capillary forces pull and align a part in place once contact is made.....	2
Figure 2. Bi-Sn phase diagram (from (28)).	6
Figure 3. EDX plot of alloy A.	6
Figure 4. Array of 20 μm diameter, 220 nm thick Cr-Ni-Au features on Si after dip coating in a 58% Bi, 42% Sn alloy.	7
Figure 5. Alloy bump height vs. diameter for alloy D on circular and square regions.....	8
Figure 6. 58Bi-Sn alloy composition vs. time for 20 μm diameter features in EG at 150 $^{\circ}\text{C}$	9
Figure 7. Bi composition vs. time for a 58Bi-Sn alloy deposited on 10, 20, and 30 μm diameter features vs. immersed in EG at 150 $^{\circ}\text{C}$	9
Figure 8. Scanning electron microscope (SEM) image and EDX results for a Bi-Sn alloy on 30 μm diameter, 200 nm thick Ni pads after 15 min in pure EG at 150 $^{\circ}\text{C}$	10
Figure 9. Bi+Pb composition vs. time for a 44.7% Bi, 8.3% Sn, 22.6% Pb, 19.1% Cd, 5% Cd alloy immersed in EG at 100 $^{\circ}\text{C}$	10
Figure 10. Bi composition of alloy (30 μm diameter features) as a function of time in various solutions at 150 $^{\circ}\text{C}$, determined by EDX.....	11
Figure 11. Bi composition of alloy (30 μm square features) as a function of time in glycerol at 180 $^{\circ}\text{C}$ with various HCl concentrations, determined by EDX.	12
Figure 12. Bi-Sn alloy composition (30 μm square features) as a function of time in 1-octanol at 180 $^{\circ}\text{C}$ at various HCl concentrations, determined by EDX.....	12
Figure 13. SEM images of a eutectic Bi-Sn bump on a 20 nm Cr, 100 nm Ni, 100 nm Au layer (the top Au layer is assumed to dissolve once the solder is deposited by dip coating).	13
Figure 14. Schematic diagrams showing how templates and parts are fabricated for self-assembly experiments, and how parts assemble on binding sites.....	14
Figure 15. Temperature rise of a vial containing 4 ml of glycerol placed in a 180 $^{\circ}\text{C}$ glycerol bath.....	15
Figure 16. Self-assembly with 100 μm diameter, 50 μm tall parts exhibiting 97% yield.	16
Figure 17. Self-assembly with 100 μm square, 50 μm tall parts exhibiting 96.5% yield.....	17
Figure 18. Self-assembly with 40 μm square, 20 μm tall parts (85% yield), and with 20 μm diameter, 10 μm tall parts (15% yield).	18
Figure 19. A template of self-assembled 40 μm square parts after sonication in isopropyl alcohol for 5 s, which removed most of the bound parts.	18

Figure 20. Templated self-assembly yield vs. contact diameters for a) parts with similar contact-part size ratios and b) different contact-part diameters; c), d) and e) show representative SEM images from the experiments in b): c) 45 μm part contacts on 45 μm template alloy contacts, d) 90 μm part contacts on 20 μm template alloy contacts, and e) 90 μm part contacts on 90 μm template alloy contacts.	19
Figure 21. Optical microscope images and SEMs of parts and templates with interconnects: a) fabricated and released parts, b) templates with recesses for self-assembly of the parts, and c) SEM showing one assembled part, allowing conductance to be measured.	21
Figure 22. Measured resistance vs. interconnect length for parts assembled on templates, where each interconnect length calculation included two 20 μm diameter self-assembled contacts, such that 340 Ω corresponded to 1.9 / $\text{m}\Omega\text{-cm}^2$	22

List of Tables

Table 1. Composition and melting point (M.P.) of metal alloys tested.	3
Table 2. Composition, boiling point (B.P.) and viscosity of self-assembly fluid environments tested.	5

Acknowledgement

The author gratefully acknowledges support for this work from the Defense Advanced Research Projects Agency (DARPA) through the U.S. Department of Defense Science, Mathematics and Research for Transformation (SMART) fellowship program.

1. Introduction

Advances in electronics and microelectromechanical systems (MEMS) continue to enable smaller, faster, cheaper, and more integrated systems. Despite this progress, efforts in the area of integration have faced significant challenges in constructing three-dimensional (3-D) structures and building heterogeneous integrated systems made of parts from incompatible microfabrication processes. This report addresses these challenges by investigating self-assembly as a means of heterogeneous integration. Although robotic “pick-and-place” techniques are currently used to integrate devices from many types of processes, the ability to efficiently handle individual parts diminishes as the size scale of the components decreases below about 300 μm (1). Our approach based on self-assembly, or the spontaneous organization of parts into larger structures via energy minimization, is an attractive solution to overcome present-day integration limitations.

Heterogeneous integration requires the placement and alignment of parts, and the formation of electrical and mechanical connections. Our self-assembly method is based on fluidic agitation and capillary forces from a molten alloy, and accomplishes all four of these heterogeneous integration tasks. The typical molten-alloy self-assembly process is shown in figure 1 and involves suspending parts in a self-assembly fluid environment where buoyancy facilitates part agitation. When an alloy-coated region of a template is liquefied by heat and makes contact with a metal binding site on another part, capillary forces bind and align the part as shown at the bottom of figure 1. Many research groups employ molten alloys at small scales for self-assembly combined with other driving mechanisms such as gravity (2, 3) or magnetic fields (4). Those using capillary forces from molten alloys exclusively (5–7) use molten alloy contacts with linear dimensions of 200 μm and larger. We would like smaller contact sizes for self-assembly, because at larger scales, it is logical to use conventional integration methods.

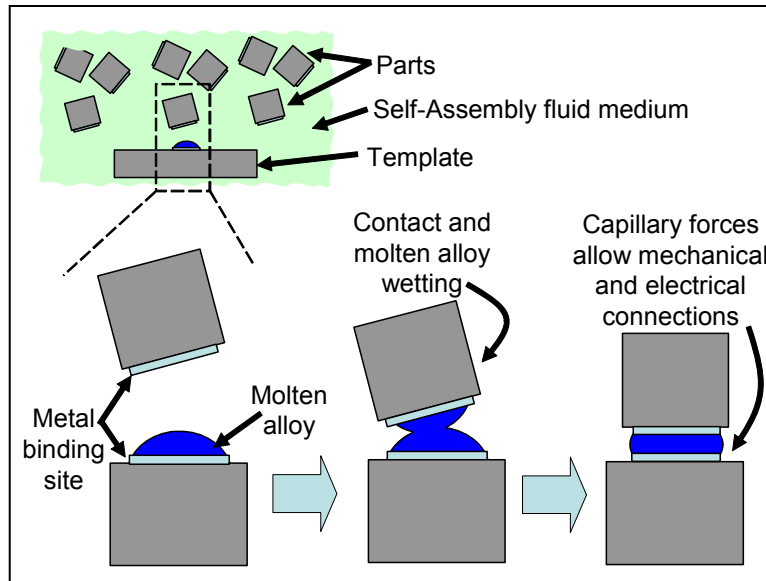


Figure 1. Schematic drawing showing how one part from a randomly agitated collection of parts will assemble on a molten alloy-coated binding site, where capillary forces pull and align a part in place once contact is made.

One reason for the large contact sizes reported in past self-assembly studies is that molten alloys typically require an acid “flux” to clean oxides off alloy surfaces, and the process of alloy oxidation and oxide reduction continually removes alloy material. Thus, it is necessary to have enough alloy material to function for an extended period of time. Another reason is the intermetallic compound (IMC) resulting from reactions between the molten alloy and the base metal, which is essential to wetting and bonding but may also consume either the base metal and/or the molten alloy. These processes ultimately limit the size scale to which self-assembled structures using a molten alloy can be miniaturized. At least one study addresses how IMCs limit the scaling of capillary based self-assembly for rotating structures out of a plane (8), but non-uniform IMC growth prevented the realization of this simple scaling argument.

The examples of self-assembly for packaging mentioned above, as well as other demonstrations of integration by molten-alloy-based self-assembly (7, 9–13), all use the five-component, eutectic alloy listed in table 1 as alloy A. The kinetics of alloy corrosion and IMC growth decrease significantly with temperature, so it appears that other researchers have avoided most problems related to these chemical processes by working with an alloy melting at 47 °C. One exception to alloy A is the use of a eutectic bismuth (Bi)-tin (Sn) alloy (alloy D in table 1), which in one study (14) was liquefied locally on a template by embedded, addressable heaters. In that study, the use of large area contacts (greater than 200 μm square) and the heating of these areas for short times appear to be successful.

Table 1. Composition and melting point (M.P.) of metal alloys tested.

Alloy	Composition (Mass Percentages)						M.P. (°C)
	Bi	Sn	Pb	In	Cd	Ag	
A	44.7	8.3	22.6	19.1	5		47
B	50	13.3	26.7		10		70
C	55.5		45.5				124
D	58	42					138
E			15	80		5	154
F				100			154

NOTE: Pb = lead, In = indium, Cd =cadmium, and Ag = silver.

A variety of alloys are used in modern flip chip bonding or die attach processes, where capillary forces enable precision alignment and mechanical/electrical connections, similar to our proposed self-assembly process. In these processes, previously deposited alloy bumps are briefly heated above the alloy melting temperature to “reflow” the alloy and form intended connections. The reflow process takes place either in a small amount of liquefied flux in the vicinity of each alloy bump, or in a gaseous, formic acid environment. The alloy bump diameter used in these applications has been shrinking from 100 μm and larger to 46 μm (15), 30 μm (16), and 25 μm (17, 18). Alloy systems include eutectic Sn-Pb, eutectic Sn-Bi, 99.3Sn-copper (Cu), and eutectic gold (Au)-Sn solder. Although these processes work well, they do not directly transfer to self-assembly, because the stochastic nature of self-assembly requires longer reflow times. Longer times at higher temperatures lead to the same difficulties in scaling molten alloy contacts as outlined previously.

Therefore, a fundamental question to answer is how small can molten alloy contacts be made for capillary force-based self-assembly? Further knowledge about scaling such contacts is of great importance to the future development of self-assembly as a viable technology for miniature packaging and integration, and this report enables such future development.

2. Alloy and Fluid Environment Experiments

2.1 Methods

To answer the question of how small contacts can be made for self-assembly, we first need to determine the right combination of alloy, base metal, and self-assembly fluid. We selected the five alloys and one pure metal in table 1, because they were readily available (from Small Parts, Inc., or Indium Corporation). Although other higher melting point alloys were also considered, the availability of fluids with boiling points above 200 °C is significantly reduced, so the choice

of alloys was restricted to those with melting points significantly below 200 °C. We first tested each alloy/metal for ease of deposition on a patterned metal template, and tested alloys A and D in a variety of self-assembly fluids for corrosion resistance.

Methods to deposit an alloy include direct solder-ball transfer, electroplating, evaporation and lift-off, screen printing of a solder paste, liquid solder jet printing, and dip coating (19) (or meniscus bumping (20)). Many of these methods require extensive development specific to the alloy, substrate, and pattern to be printed, particularly for feature sizes below about 100 μm (19). For example, in one study (16), the extensive industrial development required to deposit 30 μm diameter alloy bumps via screen printing is described. On the other hand, dip coating is easily applied to any alloy in its molten state and is attractive for rapidly testing different alloys. We followed the dip coating process used in reference 3, which involved dipping a substrate containing 200 nm/20 nm thick Au/Cr patterns in a bath of ethylene glycol (EG) heated to 90 °C, with 10–100 mM hydrochloric acid (HCl) added, and a volume of alloy A, which settles at the bottom due to its higher density. Upon retraction of the substrate from the molten alloy through the EG/alloy interface at approximately 1 cm/s, the alloy selectively wets Au regions, while the low contact angle of EG on silicon (Si) and/or silicon dioxide (SiO_2) prevents the alloy from wetting the rest of the substrate, causing it to “dewet.” We performed dip coating for the higher melting point alloys between 5 and 50 °C above the alloy melting temperature.

We fabricated metal patterns on a Si wafer by photolithography for test templates, using e-beam evaporation and liftoff in acetone. The patterns consisted of a 20-nm chromium (Cr) adhesion layer and 200 nm of Au. Latter metal combinations included 200 or 500 nm Cu; 100 or 200 nm nickel (Ni) followed by 100 nm Au; and 150 nm platinum (Pt) followed by 100 nm Au, all on top of the same Cr adhesion layer. The reason for the switch to Pt is discussed near the end of section 2.2 and had to do with Pt reacting much more slowly with Sn than Ni. We dip coated these substrates using the procedure described above. We measured height profiles using an optical profiler (Wyco model NT3300, Veeco Instruments, Woodbury, NY). Ongoing research in our group concerns the fabrication of Si parts for self-assembly into 3-D electrical networks, with a first generation design of these parts including 20 μm diameter alloy regions. Thus, the present study concerns similarly sized features.

We selected the nine fluids in table 2 to test how an alloy resisted excessive corrosion. The use of a fluid for molten-alloy-based self-assembly dictates that the liquid must have a high enough boiling point to remain a liquid beyond the alloy melting point. Fluids selected included EG; EG with sodium nitrite (NaNO_2) or sodium benzoate (SB) as anti corrosion agents (22); glycerol; hexadecane; 1-octanol; and three ionic liquids based on choline chloride (ChCl), one of which has been used for plating zinc (Zn)-Sn alloys with a variety of Sn concentrations (27). The EG:ChCl combination was selected for its lower metal oxide solubility compared to other ChCl-based ionic liquids (23). Energy-dispersive x-ray spectroscopy (EDX) (Thermo Noran EDX model 133A-3SES, Noran Instruments, Inc.) works by exciting electrons in the various energy levels of elements which are present, using the energy from a scanning electron microscope

beam. As the electrons “fall” back to their original energy levels, x-rays are emitted with an energy spectrum, which acts as a “fingerprint” for a particular element. The presence and quantity of elements may then be determined. We performed EDX at 20 kV before and after exposure to each liquid at 150 °C to reveal the composition change of the alloy “bumps” and indicated whether significant corrosion occurred. When a liquid did not significantly change the alloy composition with time, similar tests conducted with different concentrations of HCl in that liquid determined the rate at which the oxidation/reduction reactions occurred. A significant change was defined as one that caused the Bi concentration to fall below 51% or rise above 60%, with each bound corresponding to the alloy’s solidus line at 150 °C according to the Bi-Sn phase diagram shown in figure 2.

Table 2. Composition, boiling point (B.P.) and viscosity of self-assembly fluid environments tested.

Fluid	Composition		B.P. (°C)	Viscosity (cP)		Reference
	A	B		100 °C	180 °C	
A	EG		199	2.0	0.95	(21)
B	EG	0.3% NaNO ₂	~199	2.0	0.95	(22)
C	EG	2% SB	~199	2.0	0.95	(22)
D	EG	ChCl (2:1)	~199	–	–	(23)
E	ZnCl ₂	ChCl (2:1)	190	2817	362	(24)
F	urea	ChCl (2:1)	^a	14.8	2.9	(25)
G	hexadecane		287	0.92	0.61	(21)
H	1-octanol		195	0.93	0.52	(21)
I	glycerol		290	15.1	2.73	(21, 26)

NOTE: The number in parentheses refer to (A:B) molar ratios: ChCl denotes choline chloride, EG denotes ethylene glycol, and SB denotes sodium benzoate. Viscosity values at 180 °C are extrapolated from reference data using logarithmic fits.

^a Urea decomposes above about 130 °C.

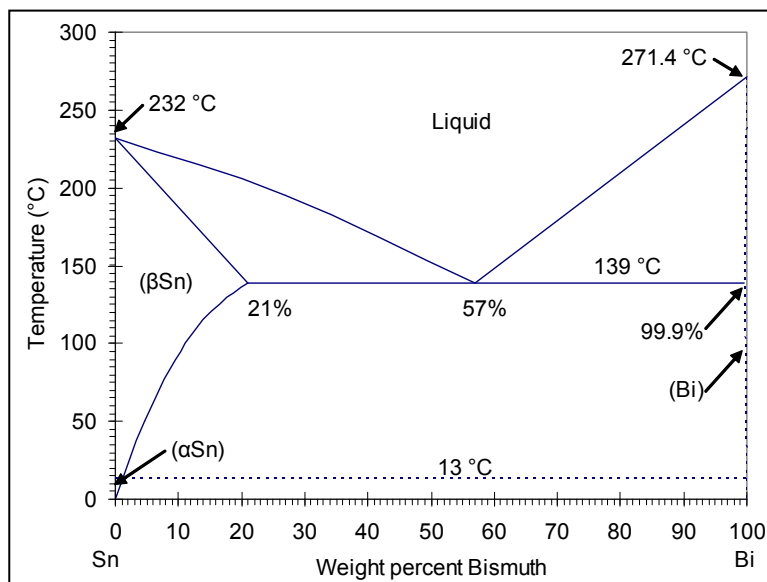


Figure 2. Bi-Sn phase diagram (from (28)).

2.2 Results and Discussion

Alloy A worked well when we dip coated 200 nm thick Au templates. However, the five-component composition of alloy A would later complicate a study of its corrosion-related properties. The EDX signals for In, Cd, and Sn were nearly indistinguishable from one another, as were the signals for Bi and Pb (see figure 3). We could only accurately determine the superposition of these two groups of elements. For example, prior to exposure to any fluid from table 2, EDX analysis of a sample of alloy A indicated 0%Bi, 2%Sn, 70%Pb, 4%In, and 24%Cd, which all differed from the reference values in table 1. But the sum of Bi+Pb=70% was close to the expected value of 67.3% (from a superposition of the expected percentages for Bi and Pb in table 1).

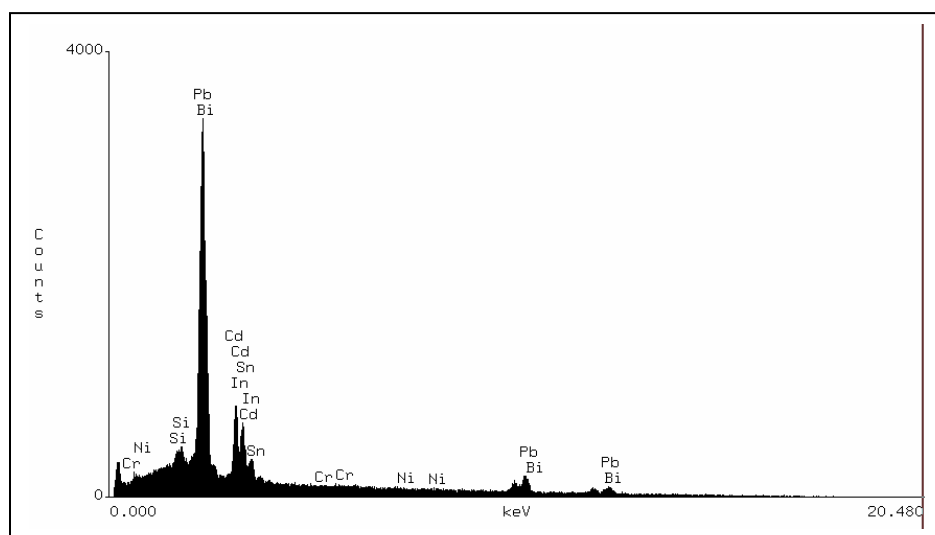


Figure 3. EDX plot of alloy A.

A move to higher melting point alloys revealed challenges associated with using thin-film base metal layers: many metals dissolve rapidly into molten alloys at elevated temperatures. For alloys B, C, and D, working at dip coating temperatures over about 100 °C, an entire 200 nm thick Au base metal layer dissolved within 2 s. We tried alloy F for which a three orders of magnitude lower Au dissolution rate is reported for Au in Pb-37Sn solder (29). However, both alloys E and F suffered from apparent excessive oxidation rates in EG, indicated by a pH level which quickly rose to near 7 within 40 s following the addition of 100 mM HCl. This excessive oxidation prevented consistent deposition with the dip coating procedure, at least with EG. A 200 nm Cu layer replacing the Au layer was an improvement for alloys B, C, and D, but this combination of alloy and base metal still resulted in less than 5% of the patterns on a substrate being successfully coated at temperatures above 150 °C, now due to rapid Cu dissolution. The yield at lower temperatures for alloy B was usually about 50%.

Nickel is an alternative base metal layer because of its low dissolution rate (30) and is commonly capped with a sacrificial Au layer to prevent Ni oxidation. The sacrificial Au layer quickly dissolves when exposed to a Sn-based molten alloy. Using a 20 nm Cr, 100 nm Ni, 100 nm Au base metal combination, alloys B, C, and D were successfully dip coated with yields above 98%. For example, figure 4 shows the results of dip coating a substrate with alloy D on 20 μm diameter features, and figure 5 shows the resulting alloy bump height as a function of diameter for alloy D on square and circular features. We selected Alloy D for the most extensive further study due to its lead-free status, reports of a low oxidation rate compared to many other solders (31–33), and for its simple, two-element composition. Both elements, Sn and Bi, were easily distinguishable from one another using EDX.

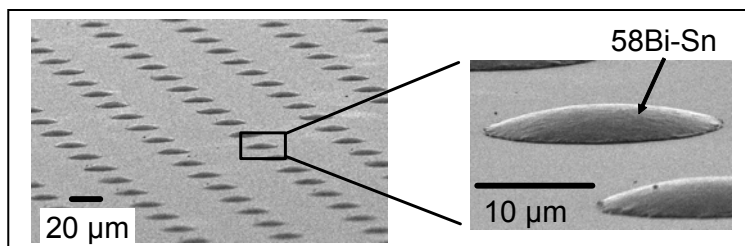


Figure 4. Array of 20 μm diameter, 220 nm thick Cr-Ni-Au features on Si after dip coating in a 58% Bi, 42% Sn alloy.

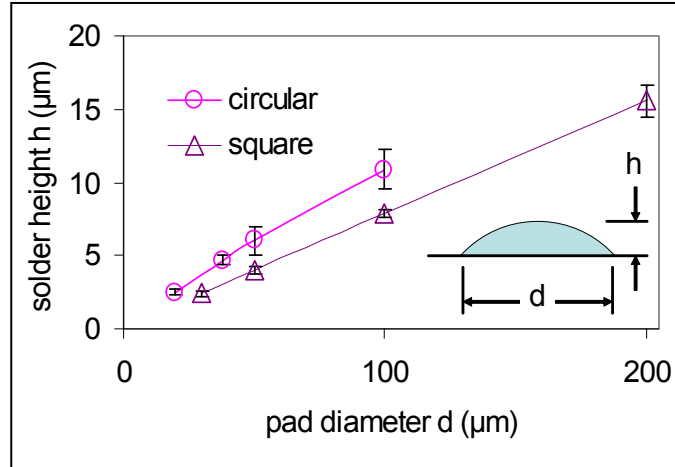


Figure 5. Alloy bump height vs. diameter for alloy D on circular and square regions.

NOTE: Lines shown for clarity.

The first liquid tested was EG, and figure 6 shows how the composition of alloy D on a Au/Ni/Cr template (100 nm Ni layer) varied with time in EG at 150 °C. The Bi concentration initially increased, while the relative amount of Sn decreased, suggesting that EG initially attacked Sn. After approximately 14 min, the Sn and Ni percentages sharply increased, accompanied by a decrease in Bi, which eventually approached zero, indicating that Bi was being attacked as well. The final atomic ratio of Ni:Sn was approximately 3:4, indicating Ni_3Sn_4 , which is the primary Ni-Sn IMC at these temperatures (34). Other IMCs are possible, such as Ni_3Sn_2 at temperatures above 240 °C (35), but at lower temperatures they are present in quantities so small that a tunneling electron microscope (TEM) is required to observe them (34). In general, IMCs between Ni and Bi do not form (36). Figure 7 shows that the initial Bi increase and decrease trend holds for various alloy diameters, and therefore various alloy volumes, with smaller volumes of solder taking less time to undergo the same composition changes.

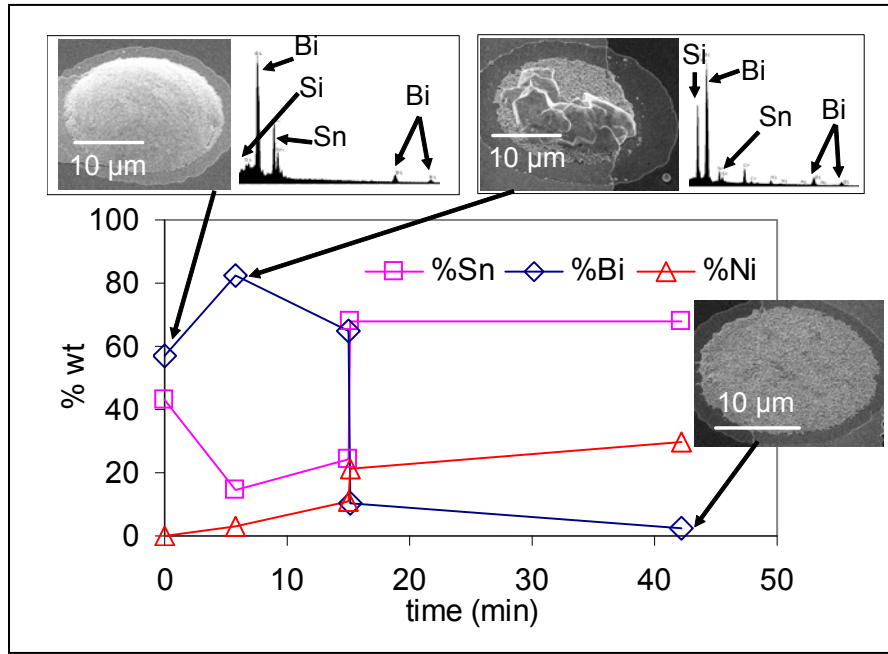


Figure 6. 58Bi-Sn alloy composition vs. time for 20 μm diameter features in EG at 150 °C.

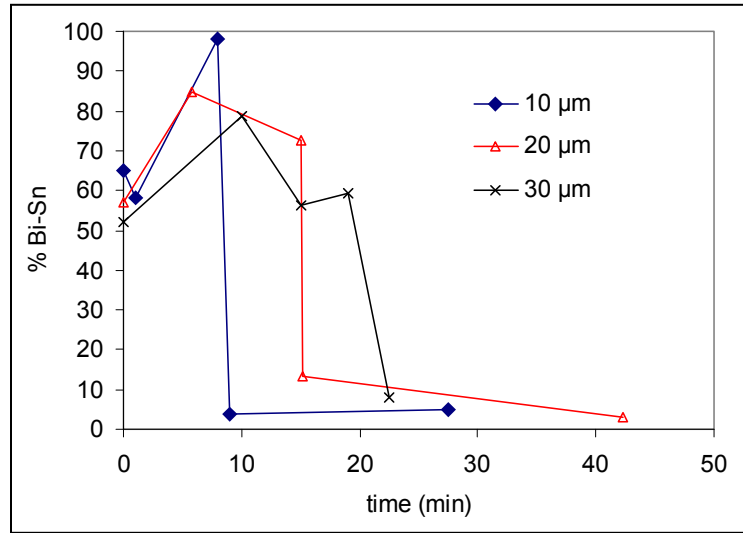


Figure 7. Bi composition vs. time for a 58Bi-Sn alloy deposited on 10, 20, and 30 μm diameter features vs. immersed in EG at 150 °C.

Figure 8 shows details of an EDX analysis on specific areas of a 30 μm diameter alloy bump after 15 min of exposure to ethylene glycol, and shows that the Bi regions often formed facet structures similar to those observed when alloy D is cooled at a slow rate (15). The facets in figure 8 likely formed not due to cooling, but due to a crossing of the solidus line of the Bi-Sn phase diagram as the relative Bi composition increased (see figure 2).

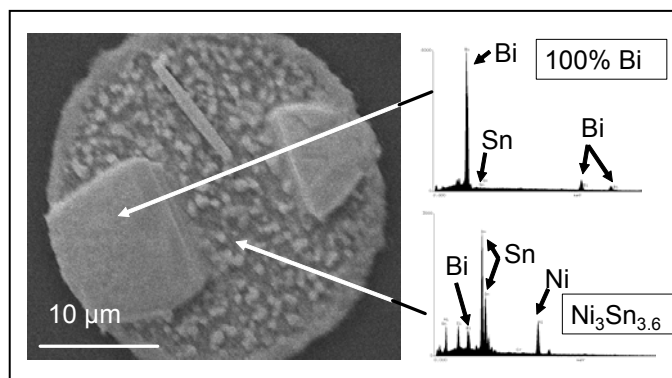


Figure 8. Scanning electron microscope (SEM) image and EDX results for a Bi-Sn alloy on 30µm diameter, 200 nm thick Ni pads after 15 min in pure EG at 150 °C.

NOTE: Facet regions consisting of 100% were left, and a substance close to Ni_3Sn_4 (3:3.6 atomic ratio of Ni:Sn) was indicated elsewhere.

Although most results in this study are from alloy D, figure 9 shows some data for how the combination of Bi and Pb in alloy A changed with time in EG. The lower operating temperature delayed corrosion, but similar behavior to that in the first few minutes of figure 6 was observed.

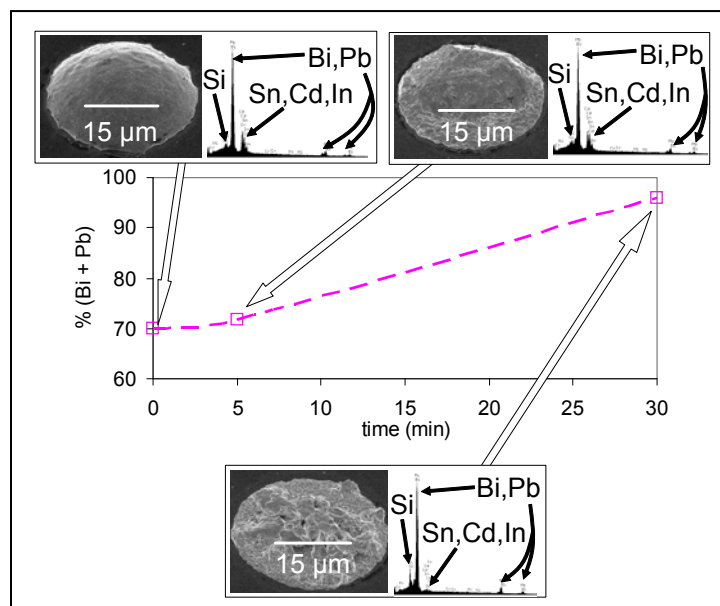


Figure 9. Bi+Pb composition vs. time for a 44.7% Bi, 8.3% Sn, 22.6% Pb, 19.1% Cd, 5% In alloy immersed in EG at 100 °C.

The Bi composition during exposure to EG and to the eight other candidate fluids from table 2 is shown in figure 10. None of the additives intended as anti-corrosion agents for EG worked well with alloy D at such elevated temperatures. The ionic liquids were also quite corrosive. Only hexadecane, glycerol, and 1-octanol did not change the alloy composition significantly for the

first 5 min, and only the first two did not impart a significant change after 25 min. We attempted the dip coating procedure described in section 2.1 with hexadecane in place of EG, and with HCl added at least 1 h prior to the experiment to allow the slow dissolution process to occur. However, the yield of correctly deposited alloy was never more than about 10%. Furthermore, a precipitate was visible on the surface of the alloy when heated in acidic hexadecane, implying that the hexadecane solution was not able to dissolve the alloy's oxide reduction product. We tried sulfuric acid and acetic acid in place of HCl in hexadecane, with similar results. Thus, glycerol and 1-octanol were selected for further study.

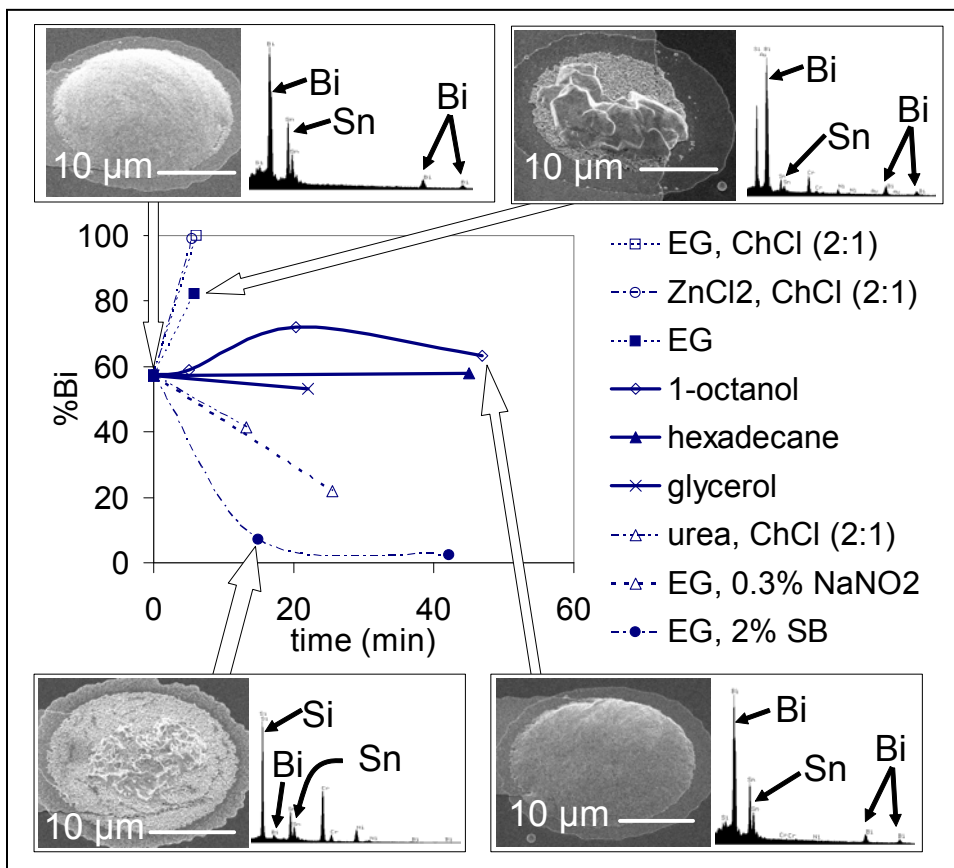


Figure 10. Bi composition of alloy (30 μm diameter features) as a function of time in various solutions at 150 $^{\circ}\text{C}$, determined by EDX.

The dashed lines in figure 10 are shown for clarity, rather than to indicate a particular trend with time. Figure 6 demonstrated the relative Bi concentration increased and then decreased due to an initial preferential reaction with Sn, so each of the data points in figure 10 could have occurred before or after this peak, if such a peak even occurred for a particular liquid. The important result is that two of the liquids tested did not change the Bi concentration for a significant period of time.

Figures 11 and 12 show how the alloy fared at different HCl concentrations in glycerol and 1-octanol at 180 °C, corresponding to a liquid regime between 36 and 70% Bi, according to the Bi-Sn phase diagram at that temperature. In general, the alloy was less affected by the same HCl concentration in glycerol when compared to 1-octanol. Small bubbles originated at alloy surfaces in 1-octanol at 180 °C with all HCl concentrations, including a case with no HCl added at all, hinting that the fluid was probably too close to its boiling point (197 °C). Knowing that bubbles would interfere with the self-assembly process and given the lesser effect of HCl on alloy composition change, we chose glycerol for further self-assembly experiments.

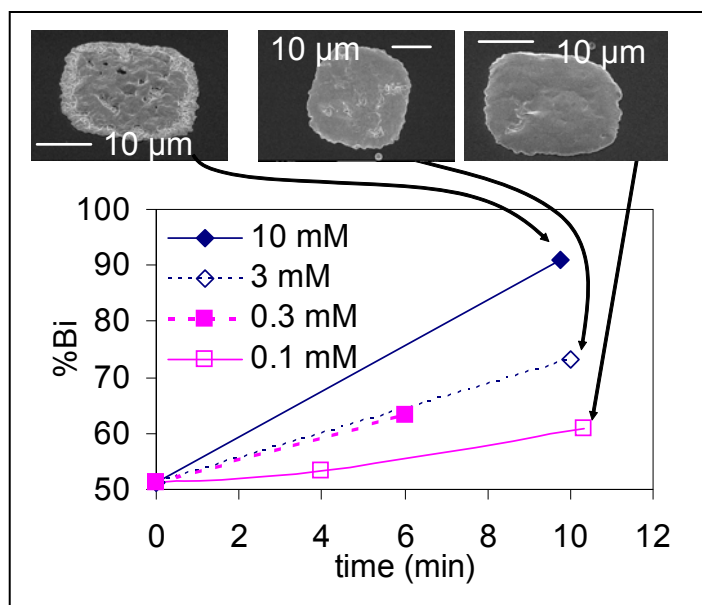


Figure 11. Bi composition of alloy (30 μm square features) as a function of time in glycerol at 180 °C with various HCl concentrations, determined by EDX.

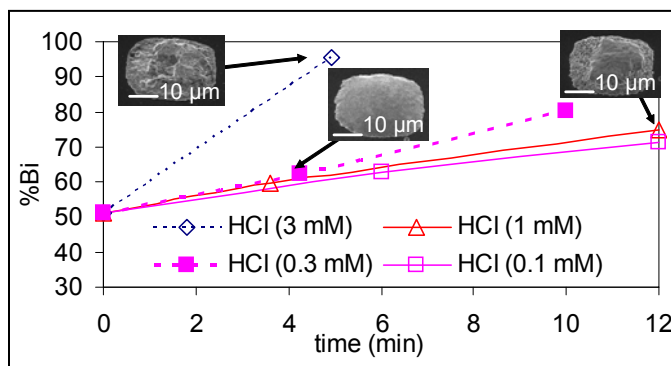


Figure 12. Bi-Sn alloy composition (30 μm square features) as a function of time in 1-octanol at 180 °C at various HCl concentrations, determined by EDX.

The templates in figures 11 and 12 had a 150 nm Pt layer instead of Ni, because the alloy dewetted from Ni after a few minutes. Such dewetting behavior has been explained for a eutectic Sn-Pb alloy on 200 nm of Ni with a titanium (Ti) adhesion layer in one study (37). In that study the Ni_3Sn_4 IMC layer completely consumes the original Ni, spalls into the alloy, and leaves only Ti. Ti has a large interfacial energy difference with respect to the alloy, which drives dewetting. In another study (38), dewetting of pure Sn on a Cu/Cr metal layer was observed, indicating that similar behavior occurs with Cr adhesion layers. The alloy was observed to dewet in figure 13b, which displayed a 60% Bi, 40% Sn composition from EDX analysis (2% standard deviation over four measurements), but is clearly dewetting from the template. Figure 13c shows the IMC that remains after EG has reacted with most of the original alloy, hinting that there is not a strong bond between the IMC and the underlying Cr. Attempts at “capping” the edge of the Ni layer with an additional 200 nm of Cr did not prevent the same dewetting behavior. The Sn-Pt IMC is a much better diffusion barrier to further IMC growth (39) and was, therefore, used in place of Ni in figures 11 and 12.

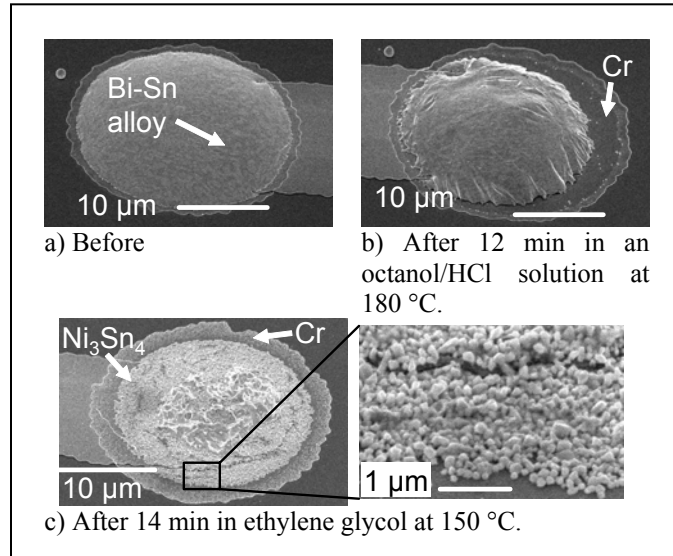


Figure 13. SEM images of a eutectic Bi-Sn bump on a 20 nm Cr, 100 nm Ni, 100 nm Au layer (the top Au layer is assumed to dissolve once the solder is deposited by dip coating).

3. Self-Assembly

3.1 Methods

With a suitable alloy and fluid environment combination, we investigated the self-assembly process. We fabricated parts for self-assembly by starting with a silicon-on-insulator (SOI) wafer having a 10, 20, or 50 μm thick device layer and a 2 μm thick silicon oxide layer. A 20 nm Cr, 150 nm Pt, and 100 nm Au metal multilayer defined by photolithography, e-beam

evaporation, and lift-off in acetone formed metal contacts on the parts. Next, we patterned a 6 μm layer of AZ4620 photoresist (AZ-Electronic Materials USA Corp., Branchburg, NJ) to define the outline of each part, hard-baked it for 4 h, and subjected the exposed Si to a deep-reactive ion etch (DRIE) down to the buried oxide. Finally, buffered-oxide etch (BOE) dissolved the buried oxide, allowing parts to detach from the handle wafer. We collected the parts with a cellulose-based filter, rinsed them extensively with de-ionized (DI) water, placed them in a 85 $^{\circ}\text{C}$ bath of EKC 830 photoresist remover (Dupont Electronic Technologies, Hayward, CA) for 20 min, and finally rinsed and transferred them to a vial of DI water. We also fabricated templates with 20 nm/150 nm/100 nm Cr/Pt/Au patterns using photolithography, e-beam evaporation, and lift-off, and coated these templates with alloy D using the dip coating procedure given in section 2.1, with a dip coating temperature of 160 $^{\circ}\text{C}$ and a 20 s immersion time in the molten alloy.

For a self-assembly experiment, we transferred parts into a vial and added a 3:7 $\text{H}_2\text{O}_2\text{:H}_2\text{SO}_4$ “piranha” solution for 1 min to insure clean metal contacts. We then diluted the acid with DI water by a factor of 10^6 , followed by a dilution with ethanol by a factor of 10^6 , and finally added 4 ml of glycerol (or 1 ml for parts smaller than 100 μm in diameter) after removing nearly all the ethanol with a pipette. We heated the mixture to 100 $^{\circ}\text{C}$ to evaporate any remaining ethanol, cooled it to room temperature, and added a template as shown in figure 14. We placed the vial in a 215 $^{\circ}\text{C}$ glycerol bath for 30 s, allowing the temperature to rise above the alloy melting point as verified by an inserted glass thermometer (see figure 15 for a 180 $^{\circ}\text{C}$ glycerol bath; the rate of temperature rise to 215 $^{\circ}\text{C}$ was similar). Once the alloy was presumed to be in a liquid state, we commenced the agitation depicted in figure 14. The aspiration and discharge of approximately 1 ml of fluid (and parts) every 1–10 s using a Pasteur pipette stirred up parts at the base of the container and allowed them to gently fall across the template. We estimated the flow velocity exiting the pipette to be 12,000 mm/s (1 ml discharged in 0.1 s through a 1 mm diameter tube), with the flow aimed at the container base rather than directly at the template (see figure 14). Assembly occurred whenever one of the parts contacted a functional alloy bump, after which capillary forces held the part in place.

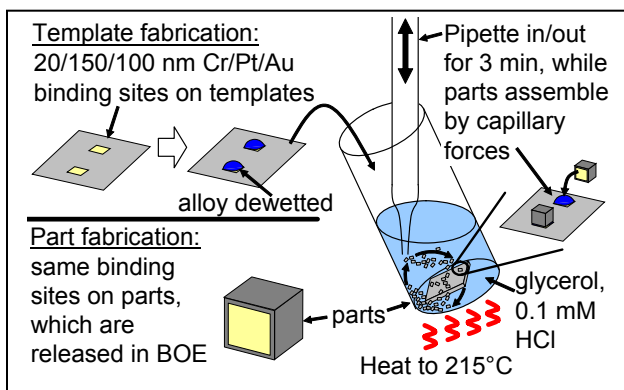


Figure 14. Schematic diagrams showing how templates and parts are fabricated for self-assembly experiments, and how parts assemble on binding sites.

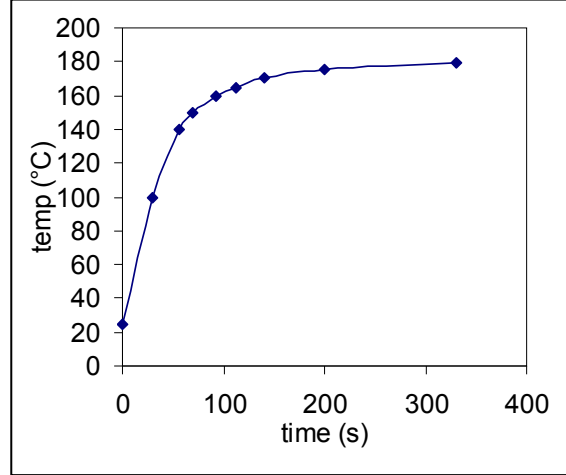


Figure 15. Temperature rise of a vial containing 4 ml of glycerol placed in a 180 °C glycerol bath.

Although capillary forces were used for self-assembly, gravitational forces brought parts into contact with binding sites. According to reference 40, the time t for the gap between a substrate and a circular plate of radius R to be reduced from ∞ to h_f is

$$t = \frac{3\pi\mu R^4}{4F} \frac{1}{h_f^2}, \quad (1)$$

where μ is the surrounding fluid viscosity and F is a constant force. If the force is due to gravity g , then equation 1 becomes

$$t = \frac{3\mu}{4\rho g T} \left(\frac{R}{h_f} \right)^2, \quad (2)$$

where ρ is the mass density difference between the fluid and part and T is the part thickness. If h_f is a particular alloy bump height (from figure 5), then the time for a part to “settle” onto its binding site increases with the square of the part’s radius or diameter. For these experiments, a 50 μm thick Si part in glycerol at 200 °C corresponds to a value of 0.0024, with a (R/h_f) ratio of about 5. Therefore, we estimated the settling time to be 0.06 s for the 100 μm diameter parts, and discharged the pipette flow every 1 s to allow parts to settle between each pulse. Equation 2 predicts settling times of 0.15 s and 0.3 s for 40 μm square, 20 μm thick parts, and 20 μm diameter, 10 μm thick parts, respectively. Therefore, we slowed the pipette flow frequency to one pulse approximately every 2.5 and 5 s.

After finishing an experiment, we cooled the container to room temperature for 5 min. We removed the template and washed it in DI water, isopropanol alcohol, and gently dried it with a stream of nitrogen. Where noted, we sonicated the template in IPA for 5–10 s to remove unbound parts. Finally, using a sample size of at least 150, the ratio of the number of assembled parts to the number of available alloy-coated binding sites constituted the self-assembly yield.

3.2 Results and Discussion

Figure 16 shows the result of assembling roughly 1500, 100 μm diameter parts on templates with 90 μm diameter molten alloy contacts. After 2.5 min of agitation, with approximately 1 Hz fluidic flow pulses, the yield was near 97%. Longer assembly times did not increase the yield significantly, probably due to the alloy bumps changing according to figure 11, but a shorter time of 1.5 min decreased the yield to 81%. Experiments similar to those in figure 16 resulted in observed yields of 96.7% and 96.3%, and when 100 μm square parts were used with the same procedure, the yield was 96.5% as shown in figure 17. We obtained the results shown in figures 16 and 17 after 5–10 s of ultrasonic agitation in isopropyl alcohol to remove unbound parts, as described in section 2.1.

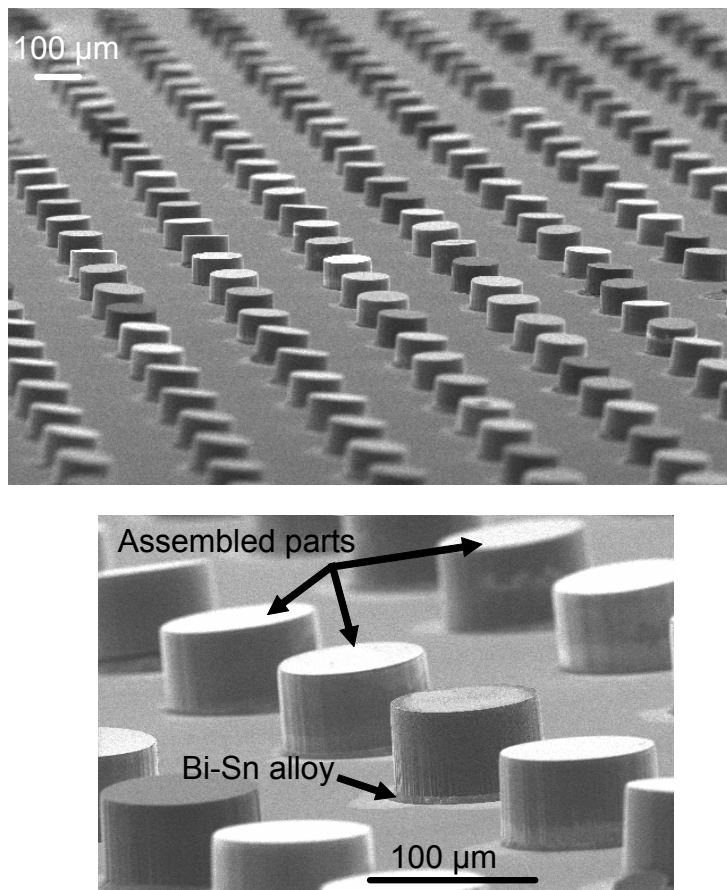


Figure 16. Self-assembly with 100 μm diameter, 50 μm tall parts exhibiting 97% yield.

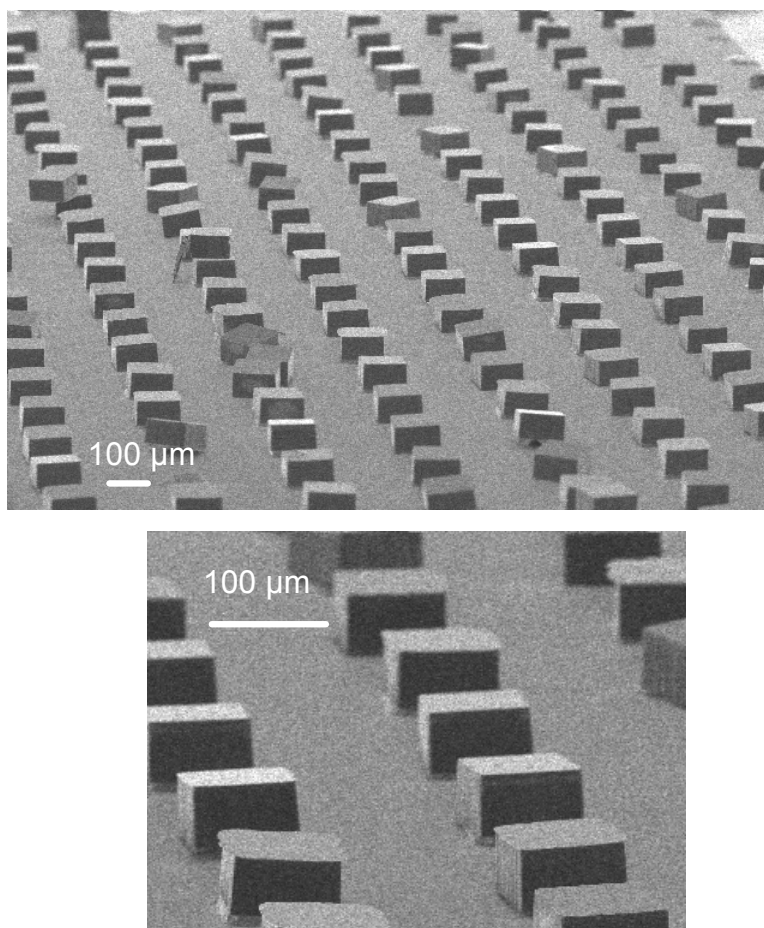


Figure 17. Self-assembly with 100 μm square, 50 μm tall parts exhibiting 96.5% yield.

Additional experiments with 100 μm and larger parts involved 100 μm square, 10 μm thick parts, at volume fractions of 2.5×10^{-5} , 2.5×10^{-4} , and 5×10^{-3} , all in 1-octanol. The yields were 3%, 15%, and 30%, respectively, indicating that the more parts present, the better the yield. Also in 1-octanol, yields at HCl concentrations of 3 mM, 1 mM, 0.3 mM, and 0.1 mM (corresponding to pH levels of 2.5, 3.0, 3.5, and 4.0) were 30%, 70%, 85%, and 30%, respectively. Thus, the yield improved with lower HCl concentration, down to a point at which the acid failed to adequately clean alloy surfaces. When using glycerol, we obtained the best results at pH=4.0, but did not try lower HCl concentrations. We performed these experiments before the final cleaning procedure and before the final choice of glycerol as the self-assembly fluid, so observed yields were lower. But the results show how changing part concentration or HCl concentration, while holding other variables constant, affected the outcome.

Moving down in scale, figure 18 shows the assembly of 40 μm square parts at 84% yield (approximately 5000 assembled in 2.5 min), and 20 μm diameter parts at 15% yield. In these tests, the total part to container fluid volume ratio was 0.003 and 0.01 for the 40 μm and 20 μm sized parts, which was similar to the experiments for 100 μm parts in figure 16 (0.01). The area ratio between part and template binding sites, or the part number to binding site number ratio, was 17 and 333 for the 40 μm , and 20 μm parts, respectively (compared to 81 for the 100 μm parts). As shown in figure 19, sonication was too violent for the 40 μm square bound parts in figure 18, even after the alloy had cooled to room temperature. Figure 20a summarizes the results from these experiments.

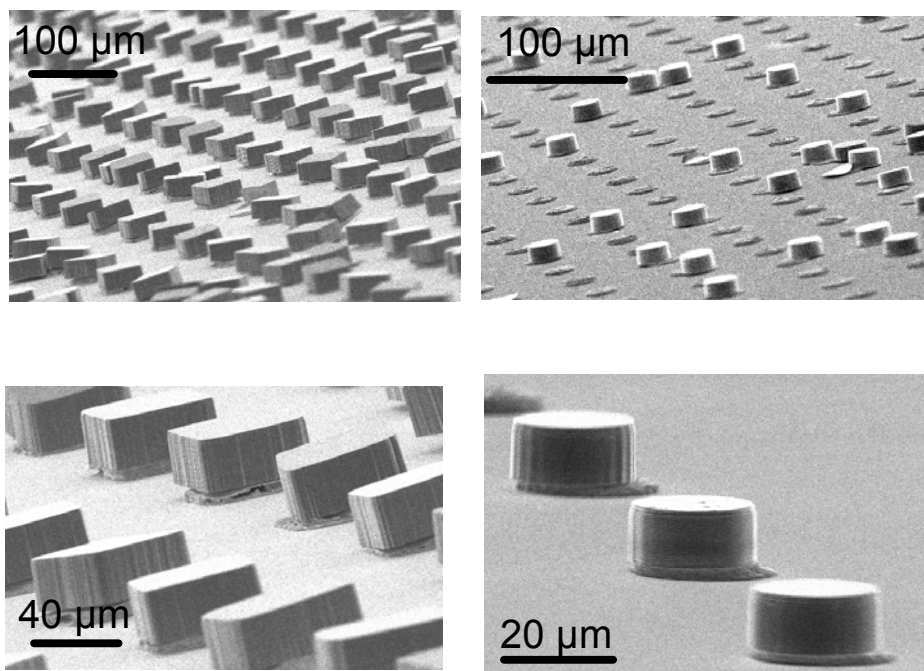


Figure 18. Self-assembly with 40 μm square, 20 μm tall parts (85% yield), and with 20 μm diameter, 10 μm tall parts (15% yield).

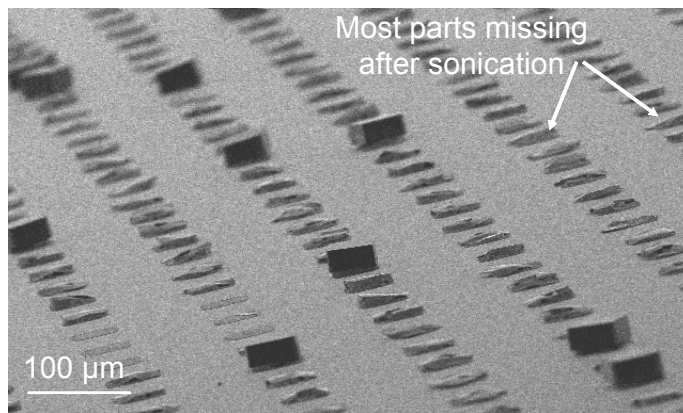


Figure 19. A template of self-assembled 40 μm square parts after sonication in isopropyl alcohol for 5 s, which removed most of the bound parts.

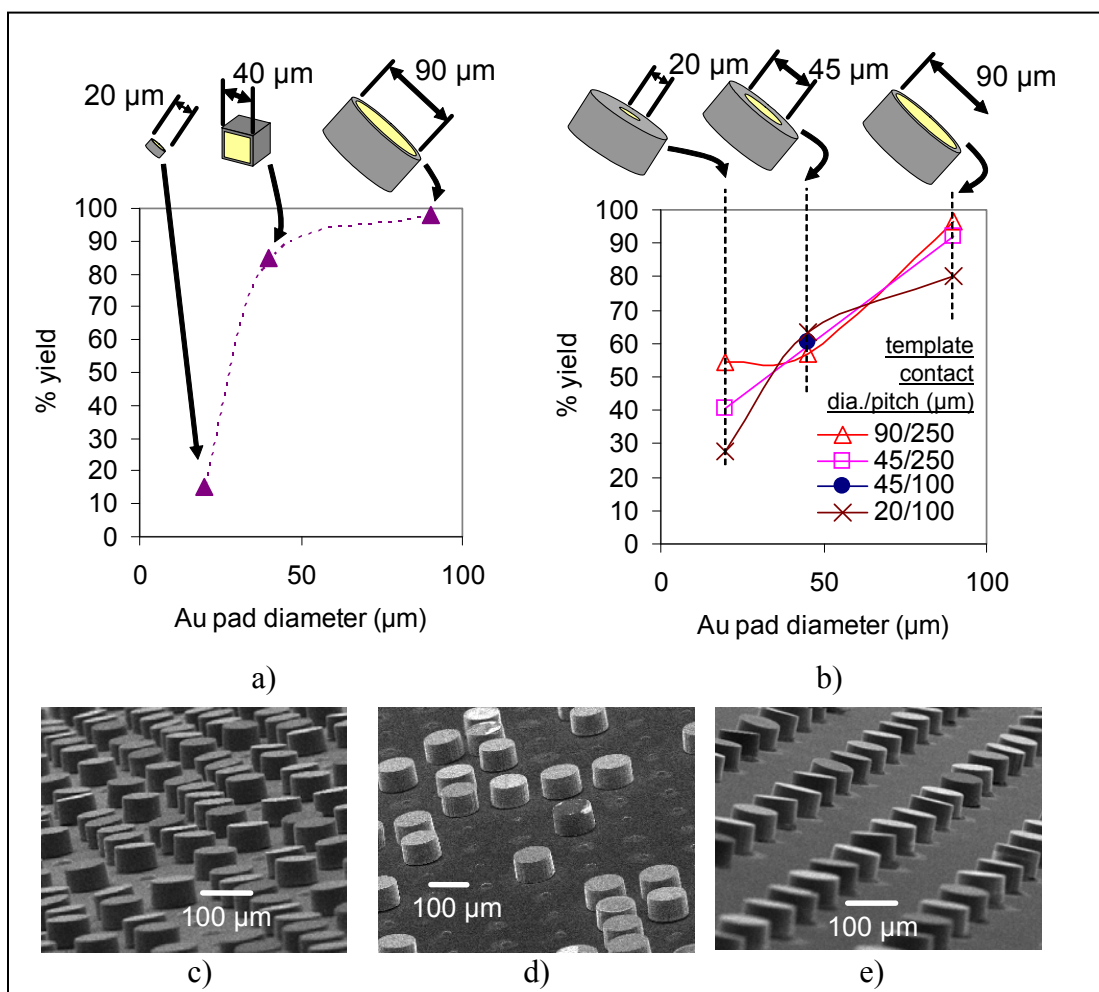


Figure 20. Templated self-assembly yield vs. contact diameters for a) parts with similar contact-part size ratios and b) different contact-part diameters; c), d) and e) show representative SEM images from the experiments in b): c) 45 μm part contacts on 45 μm template alloy contacts, d) 90 μm part contacts on 20 μm template alloy contacts, and e) 90 μm part contacts on 90 μm template alloy contacts.

To investigate why the yield dropped so dramatically with 20 μm parts, figure 20b shows a collection of results from experiments with identically-sized, 100 μm diameter parts with different contact pad diameters. We self-assembled each type of part under similar conditions on templates with the three different alloy contact diameters and pitches indicated in the legend of the figure. We performed each of the experiments in figure 20b only once and did not strictly hold the template contact pitch constant, which lead to a higher required packing density for the smaller pitch templates. Still, it is possible to speculate on the mechanisms causing the observed assembly yield in these experiments, and the differences between figure 20a and b.

At least three effects are in operation as the contact and/or part size decreases: 1) there is less capillary force available to hold parts, 2) the drag force on the parts decreases, and 3) the alloy degrades faster. For the first effect listed, the force of a capillary bond is a function of distance

between the surfaces being joined by the bond and the curvature of the fluid interface at each point in space. The exact force is difficult to determine analytically, but we determined a rough estimate by the product of the surface tension γ and the distance of the line around which it acts. For example, the force for a circular contact surface of diameter d_c is

$$F_\gamma = \gamma 2\pi d_c. \quad (3)$$

For the second effect listed, the low Reynolds number drag force on a solid, spherical particle of diameter d is given by

$$F_D = 3\pi\mu v_f d \quad (4)$$

where μ and v_f are the viscosity and relative velocity of the neighboring fluid, respectively.

We approximated the drag force of an arbitrary-shaped particle by equation 4 with the longest dimension substituted for d (41). It is apparent from equations 3 and 4 that both the capillary force and the drag force are proportional to a characteristic length, d .

For the case of figure 20a, where contact and part diameters were scaled similarly, we calculated $F_\gamma / F_D \approx 8.3$ using an estimated alloy surface tension of 300 $\mu\text{N}/\text{mm}$ (42), a fluid viscosity of 0.002 $\text{Pa}\cdot\text{s}/\text{mm}^3$, and a maximum fluid velocity of 12,000 mm/s . Therefore, capillary forces were approximately an order of magnitude greater than drag forces, and the sharp drop-off in yield with 20 μm diameter parts in figure 20a can only be attributed to the third effect listed—alloy degradation. The fact that 20 μm diameter contacts in figure 20b resulted in lower yields than parts with larger contacts also supports this argument. For the case of figure 20b, part size was held constant (100 μm diameter), and the ratio $F_\gamma / F_D \approx 8.3d_c / d$. For the 20 μm diameter contacts, $F_\gamma / F_D \approx 1.7$, indicating that the fluidic drag force may have approached the same magnitude as the capillary force. Therefore, the more linear relationship between yield and part contact size in figure 20b may be attributed to the linear relationship between capillary forces and fluidic forces.

It should be noted that between each fluidic agitation pulse, the settling time under gravitational forces may explain why the smaller contacts did not work as well. The (R/h_f) ratio of equation 2 remained constant for the experiments in figure 20a, assuming h_f changed proportionally with the contact size as indicated empirically by figure 5. However, the (R/h_f) ratio increased from 5 to 20 when going from 90 μm to 20 μm diameter contacts on the 100 μm diameter parts, so the predicted settling time under gravity increased from 0.06 s to about 1 s. Although the frequency of fluidic pulses was dropped to 0.1 Hz, it may not have been slow enough to allow the assembly to approach a higher yield. Of course, the even lower yield observed by 20 μm diameter parts on 20 μm diameter contacts is not explained by these arguments, but these brief calculations are presented to illustrate the many factors that must be accounted for in these types of experiments.

3.3 Verification of Electrical Connectivity

Figure 21a shows parts fabricated using methods similar to those described for single-contact, circular or square parts. The difference was that prior to the deposition of the Cr/Pt/Au contact layer, we evaporated a 200 nm Cr interconnect layer and patterned it by lift-off in acetone. We also fabricated templates using a 5 μm DRIE step followed by a 100 nm isolation layer of SiO_2 deposited by plasma-enhanced chemical vapor deposition (PECVD). As for the parts, we deposited similar interconnect and alloy contact layers. Before depositing solder alloy on a template, we evaporated a 100 nm of Au to insure that the alloy would wet the entire substrate. When we dipped the Au-coated substrate through a 160 $^\circ\text{C}$ EG/molten alloy interface, most of the Au dissolved so that the alloy was left only at the prescribed locations. A close-up view of one of the template recesses is shown in figure 21b.

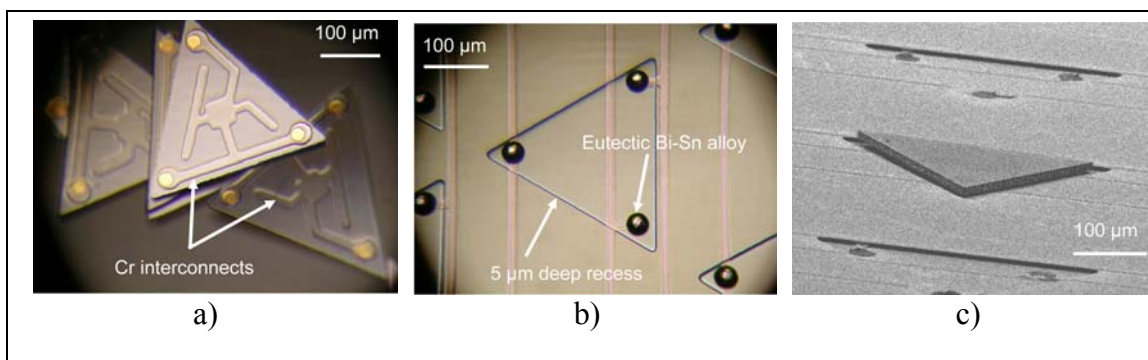


Figure 21. Optical microscope images and SEMs of parts and templates with interconnects: a) fabricated and released parts, b) templates with recesses for self-assembly of the parts, and c) SEM showing one assembled part, allowing conductance to be measured.

We self-assembled the triangular parts with 20 μm contacts on these templates with the same methods described elsewhere in this report, and a close up view of one assembled part is shown in figure 21c. Although the yield was about 15% for a template with 100 recesses, 85% of the contacts on those assembled part (three per part) showed electrical connectivity. A plot of measured interconnect length vs. resistance is given in figure 22, where each interconnect length calculation included a trip through one self-assembled contact, through the assembled part, and back down through another self-assembled contact. A linear fit by the least squares method is also shown, where the slope is the resistance per unit length of the interconnect lines. The offset, or y-intercept, of figure 22 may be interpreted as a series resistance of the probe contacts and the two self-assembled alloy contacts encountered along each interconnect length calculation. Thus, assuming the probe contact resistance to be negligible, the resistance of a single contact was 170 Ω . For an area associated with each 20 μm diameter contact, the conductance per unit area was 1.9 / $\text{m}\Omega\text{-cm}^2$.

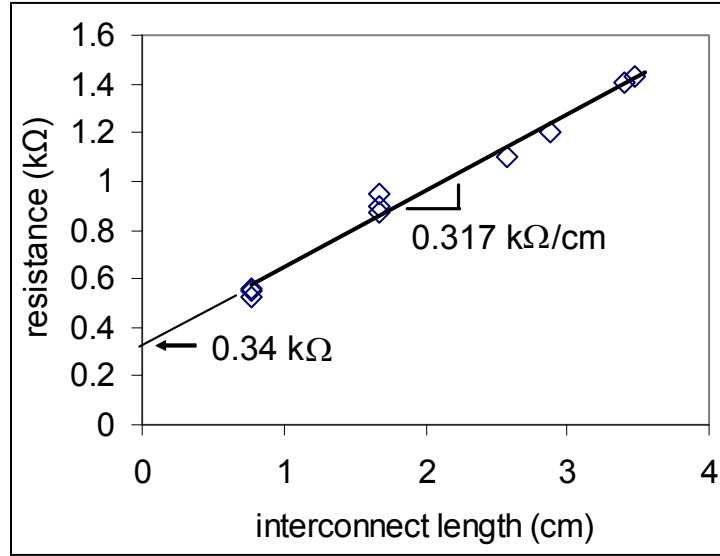


Figure 22. Measured resistance vs. interconnect length for parts assembled on templates, where each interconnect length calculation included two 20 μm diameter self-assembled contacts, such that 340 Ω corresponded to 1.9 $/\text{m}\Omega\text{-cm}^2$.

This value is on the same order of magnitude as 3 $/\text{m}\Omega\text{-cm}^2$ for 40 μm square self-assembled contacts in a previously mentioned study (3) (using the 47 $^{\circ}\text{C}$ melting point alloy in table 1), and 1.4 $/\text{m}\Omega\text{-cm}^2$ for 155 μm diameter eutectic Pb-Sn, contacts used in a die-attach application (43). In another study (44), four-point-probe structures are used to measure the contact resistance of spherical 25 μm diameter, 99.3Sn-Cu alloy bumps used in a die-attach style, chip stacking application. We infer from measurements in that study (44) a conductance per unit area of 6800 $/\text{m}\Omega\text{-cm}^2$, which is much higher than our and others' measured values. Future work should focus on reducing this contact resistance, starting first with an investigation of spherical alloy bumps.

4. Conclusion and Future Directions

In conclusion, self-assembly using a molten alloy works well with parts down to the 40 μm size scale, with correspondingly small molten alloy contacts. The investigation of six alloys or pure metals and nine possible fluid environments demonstrates that while only one successful combination was found, the information about which combinations did not work is equally valuable and gives insight into the mechanisms which prevent further scaling down in size. We generally found Sn-based alloys to be highly susceptible to corrosion at elevated temperatures above each alloy's melting point, with Sn being the primary component to corrode and also to react with the underlying base metal. These processes change the composition of the remaining alloy, and ultimately limit the size to which contacts for capillary force based self-assembly can

be made. By selecting a eutectic Sn-Bi alloy and glycerol, we demonstrated the self assembly of 1500 100 μm parts and 5000 40 μm parts, each in about 2.5 min. We measured the conductance per unit area for 20 μm diameter, 2.5 μm high alloy contacts at 1.9 $\text{m}\Omega\text{-cm}^2$.

Although we found the 40 μm size scale to be a limit for these particular experimental conditions, it is possible that smaller contacts with larger surface-to-volume ratios may also work, because the corrosion process likely depends on exposed surface area. The molten alloy contacts in this study were fabricated by a dip coating and dewetting process, which resulted in low profile depositions and small height-to-planar dimension ratios. For example, the circular contacts in this study had height-to-diameter ratios of approximately 0.1, so the volume-to-area ratio for a 40 μm diameter contact was approximately 2 μm . A 12 μm spherical alloy bump has the same volume-to-area ratio, so this alloy contact may work as well as a 40 μm diameter, low profile alloy bump formed by dip coating. As hinted at the end of section 3.3, spherical alloy bumps may also reduce the electrical contact resistance. Future work on self-assembled contacts should therefore include the fabrication of spherical alloy bumps, perhaps by electroplating.

The results of this study enable continued work on self-assembly with parts incorporating molten alloy contacts. The knowledge gained about how small contacts can be made and still function for self-assembly allows us to continue work toward a 3-D, self-assembled electrical circuit architecture at increasingly smaller size scales.

References

1. Morris, C. J.; Stauth, S.A.; Parviz, B.A. Self-assembly for micro and nano scale packaging: steps toward self-packaging. *IEEE Trans. Adv. Packag.* **2005**, *28*, 600–611.
2. Stauth, S.; Parviz, B.A. Self-assembled silicon networks on plastic. *Proceedings of the 13th Int. Conf. on Solid State Sens. Actuators (Transducers '05)*, Seoul, Korea, 2005, 964–967.
3. Stauth, S. A.; Parviz, B.A. Self-assembled single-crystal silicon circuits on plastic. *Proceedings of the Natl. Acad. Sci.* , **2006**, *103*, 13922–13927.
4. Ye, H.; Gu, Z.; Yu, T.; Gracias, D.H. Integrating nanowires with substrates using directed assembly and nanoscale soldering. *IEEE Transactions on Nanotechnology* **2006**, *5*, 62 – 6.
5. Zheng, W.; Buhlmann, P.; Jacobs, H.O. Sequential shape-and-solder-directed self-assembly of functional microsystems. *Proceedings of the National Academy of Sciences of the United States of America*, **2004**, *101*, 12814–12817.
6. Zheng, W.; Jaehoon, C.; Jacobs, H.O. Fluidic heterogeneous microsystems assembly and packaging. *J. of Microelectromechanical Systems* **2006**, *15*, 864–870.
7. Jacobs, H.O.; Tao, A.R.; Schwartz, A.; Gracias, D.H.; Whitesides, G. M. Fabrication of a cylindrical display by patterned assembly. *Science* **2002**, *296*, 323 – 5.
8. Harsh, K. F. Bright, V.M.; Lee, Y. C. Study of micro-scale limits of solder self-assembly for MEMS. *Proceedings from 50th Electronic Components and Technology Conference (ECTC)*, 2000, 1690–1695.
9. Gracias, D. H.; Tien, J.; Breen, T. L.; Hsu, C.; Whitesides, G. M. Forming electrical networks in three dimensions by self-assembly. *Science* **2000**, *289*, 1170–1172.
10. Gracias, D. H.; Tien, J.; Whitesides, G. M. Self-assembled electrical networks. U.S. Patent No. 7,007,370, 2006.
11. Gracias, D. H.; Boncheva, M.; Omoregie, O.; Whitesides, G. M. Biomimetic self-assembly of helical electrical circuits using orthogonal capillary interactions. *Applied Physics Letters* **2002**, *80*, 2802–2804.
12. Boncheva, M.; Gracias, D. H.; Jacobs, H. O.; Whitesides, G. M. Biomimetic self-assembly of a functional asymmetrical electronic device. *Proceedings of the National Academy of Sciences of the United States of America*, **2002**, *99*, 4937– 40.

13. Breen, T.L. Tien, J.; Oliver, S.R.J.; Hadzic, T.; Whitesides, G.M. Design and self-assembly of open, regular, 3D mesostructures. *Science* **1999**, *284*, 948–952.
14. Chung, J.; Zheng, W.; Hatch, T.J.; Jacobs, H.O. Programmable Reconfigurable Self-Assembly: Parallel Heterogeneous Integration of Chip-Scale Components on Planar and Nonplanar Surfaces. *J. Microelectromech. Sys.* **2006**, *15*, 457–464.
15. Kang, U.-B.; Kim, Y.-H. The microstructure characterization of ultrasmall eutectic Bi-Sn solder bumps on Au/Cu/Ti and Au/Ni/Ti under-bump metallization. *J. of Electronic Materials* **2004**, *33*, 61–9.
16. Jackson, G.J.; Hendriksen, M.W.; Kay, R.W.; Desmulliez, M.; Durairaj, R.K.; Ekere, N.N. Sub process challenges in ultra fine pitch stencil printing of type-6 and type-7 Pb-free solder pastes for flip chip assembly applications *Soldering & Surface Mount Technology* **2005**, *17*, 24–32.
17. Gan, H.; Wright, S.L.; Polastre, R.; Buchwalter, L.P.; Horton, R.; Andry, P.S.; Patel, C.; Tsang, C.; Knickerbocher, J.; Sprogis, E.; Pavlova, A.; Kang, S.K.; Lee, K.W. Pb-free Micro-joints (50 μm pitch) for the Next Generation Micro-systems: the Fabrication, Assembly and Characterization. *Proceedings of the IEEE Electronic Components and Technology Conference*, 2006, 1210–1215.
18. Knickerbocker, J.U.; Patel, C.S.; Andry, P.S.; Tsang, C.K.; Buchwalter, L.P.; Sprogis, E.J.; Gan, H.; Horton, R.R.; Polastre, R.J.; Wright, S.L.; Cotte, J.M. 3-D Silicon Integration and Silicon Packaging Technology Using Silicon Through-Vias. *IEEE Journal of Solid-State Circuits* **2006**, *41*, 1718–1725.
19. Lee, N.-C. Reflow Soldering Processes and Troubleshooting: SMT, BGA, CSP and Flip Chip Technologies. *Newnes* 2002.
20. Aschenbrenner, R.; Kallmayer, C.; Mießner, R.; Reichl, H. High Density Assembly on Flexible Substrates. *Proceedings of the Third International Symposium on Electronic Packaging Technology*, Beijing, China, 1998, 371–379.
21. Suzuki, T.; Ebert, R.U.; Schuurmann, G. Application of Neural Networks to Modeling and Estimating Temperature-Dependent Liquid Viscosity of Organic Compounds. *J. of Chemical Info. and Modeling* **2001**, *41*, 776–790.
22. Rozenfeld, I.L. v. *Corrosion Inhibitors*; translation of Ingibitory Korrozii, McGraw-Hill, 1981.
23. Abbott, A.P.; Capper, G.D.; Davies, L.; McKenzie, K.J.; Obi, S.U. Solubility of Metal Oxides in Deep Eutectic Solvents Based on Choline Chloride. *J. of Chemical and Engineering Data* **2006**, *51*, 1280–1282.

24. Abbott, A.P.; Capper, G.; Davies, D.L.; Rasheed, R. Ionic Liquids Based upon Metal Halide/Substituted Quaternary Ammonium Salt Mixtures. *Inorganic Chemistry* **2004**, *43*, 3447–3452.
25. Abbott, A.P.; Capper, G.; Davies, D.L.; Rasheed, R.K.; Tambyrajah, V. Novel solvent properties of choline chloride/urea mixtures. *Chemical Communications* **2003**, 70–71.
26. Chen, Y.M.; Pearlstein, A.J. Viscosity-temperature correlation for glycerol-water solutions. *Industrial & Engineering Chemistry Research* **1987**, *26*, 1670–1672.
27. Abbott, A.P.; Capper, G.; Davies, D.L.; Rasheed, R.K.; Tambyrajah, V. Novel ambient temperature ionic liquids for zinc and zinc alloy electrodeposition. *Transactions of the Institute of Metal Finishing* **2001**, *79*, 204–206.
28. Massalski, T.B.; Okamoto, H.; Subramanian, P.R.; Kacprzak, L. *Binary Alloy Phase Diagrams*, ASM International, Materials Park, OH, 1990.
29. Lee, J.-H.; Eom, Y.-S.; Choi, K.-S.; Choi, B.-S.; Yoon, H.-G.; Moon, J.-T.; Kim, Y.-S. Reaction characteristics of the In-15Pb-5Ag solder with a Au/Ni/Cu pad and their effects on mechanical properties. *J. of Electronic Materials* **2004**, *33*, 277–82.
30. Wassink, R.J.K. *Soldering in Electronics*, Electrochemical Publications Limited, 1984.
31. Giacomo, G.D.; Granato, K.L.; Shaukatullah, H.; Casullo, F.; Guarnieri, R. Oxidation kinetics of Bi-Sn eutectic films and thermal contact resistance. *Proceedings from International Symposium on Microelectronics*, Minneapolis, MN, USA, 1987, 587 – 93.
32. Giacomo, G.D. Oxidation of Pb-Sn eutectic solder and degradation of thermal contact resistance. *Proceedings of the 1986 International Symposium on Microelectronics*, Atlanta, GA, 1986, 322–7.
33. Konetzki, R.A.; Zhang, M.X.; Sluzewski, D.A.; Chang, Y.A. Oxidation of (Pb, Sn) and (Pb, In) alloys. *J. of Electronic Packaging* **1990**, *112*, 175–8.
34. Ghosh, G. Interfacial microstructure and the kinetics of interfacial reaction in diffusion couples between Sn-Pb solder and Cu/Ni/Pd metallization. *Acta Materialia* **2000**, *48*, 3719–3738.
35. Bader, S.; Gust, W.; Hieber, H. Rapid formation of intermetallic compounds interdiffusion in the Cu-Sn and Ni-Sn systems. *Acta Metallurgica et Materialia* **1995**, *43*, 329–337.
36. Lee, M.S.; Liu, C. M., Kao, C.R. Interfacial reactions between Ni substrate and the component Bi in solders. *J. of Electronic Materials* **1999**, *28*, 57–62.

37. Kim, P.G.; Jang, J.W.; Lee, T.Y.; Tu, K.N. Interfacial reaction and wetting behavior in eutectic SnPb solder on Ni/Ti thin films and Ni foils. *J. of Applied Physics* **1999**, *86*, 6746–6751.
38. Liu, C.Y.; Kim, H.K.; Tu, K.N.; Totta, P.A. Dewetting of molten Sn on Au/Cu/Cr thin-film metallization. *Applied Physics Letters* **1996**, *69*, 4014–4016.
39. Kuhmann, J.F.; Chiang, C.H.; Harde, P.; Reier, F.; Oesterle, W.; Urban, I.; Klein, A. Pt thin-film metallization for FC-bonding using SnPb60/40 solder bump metallurgy. *Materials Science & Engineering, A: Structural Materials: Properties, Microstructure and Processing* **1998**, *242*, 22–5.
40. Fuller, D.D. *Theory and Practice of Lubrication for Engineers*, John Wiley & Sons, 1984.
41. White, F.M. *Viscous Fluid Flow*, 2nd ed.; McGraw-Hill, Inc., New York, NY, 1991.
42. Lee, N.-C.; Bixenman, M. Flux technology for lead-free alloys and its impact on cleaning. *Proceedings from 27th Annual IEEE/CPMT/SEMI International Electronics Manufacturing Technology Symposium*, San Jose, CA, **2002**, 316–22.
43. Tsou, C.F.; Huang, Y.S. Silicon-based packaging platform for light-emitting diode. *IEEE Transactions on Advanced Packaging*, **2006**, *29*, 607–614, A.
44. Wright, S.L.; Polastre, R.; Gan, H.; Buchwalter, L.P.; Horton, R.; Andry, P.S.; Sprogis, E.; Patel, C.; Tsang, C.; Knickerbocher, J. Lloyd, J.R.; Sharma, A. Sir-Jayantha, M.S. Characterization of Micro-Bump C4 Interconnects for Si-Carrier SOP Applications. *Proceedings from IEEE Electronic Components and Technology Conference*, **2006**, 633–640.

Acronyms

3-D	three-dimensional
Ag	silver
Au	gold
B.P.	boiling point
Bi	bismuth
BOE	buffered-oxide etch
Cd	cadmium
ChCl	choline chloride
Cr	chromium
Cu	copper
DARPA	Defense Advanced Research Projects Agency
DI	de-ionized
DRIE	deep-reactive ion etch
EDX	energy-dispersive x-ray spectroscopy
EG	ethylene glycol
HCl	hydrochloric acid
IMC	intermetallic compound
In	indium
M.P.	melting point
MEMS	microelectromechanical systems
NaNO ₂	sodium nitrite
Ni	nickel
Pb	lead
PECVD	plasma-enhanced chemical vapor deposition

Pt	platinum
SB	sodium benzoate
SEM	scanning electron microscope
Si	silicon
SiO ₂	silicon dioxide
SMART	Science, Mathematics and Research for Transformation
Sn	tin
SOI	silicon-on-insulator
Ti	titanium
TEM	tunneling electron microscope
Zn	zinc

Distribution List

ADMNSTR	Copies
DEFNS TECHL INFO CTR	1 elec
DTIC OCP (ELECTRONIC COPY)	
8725 JOHN J KINGMAN RD STE 0944	
FT BELVOIR VA 22060-6218	
US ARMY RSRCH LAB	9
IMNE ALC IMS MAIL & RECORDS MGMT	
AMSRD ARL D J M MILLER	
AMSRD ARL CI OK TL TECHL LIB (2 COPIES)	
AMSRD ARL CI OK T TECHL PUB (2 COPY)	
AMSRD ARL SERL C MORRIS (3 COPIES)	
2800 POWDER MILL ROAD	
ADELPHI MD 20783-1197	
US ARMY RESEARCH LAB	1
AMSRD CI OK TP TECHL LIB	
ATTN T LANDFRIED	
APG MD 21005-5066	
TOTAL	11 (10 HCs and 1 elec)